Elsevier Editorial System(tm) for Combustion and Flame
Manuscript Draft

Manuscript Number:

Title: Transported PDF modeling of pulverized coal jet flames

Article Type: Full Length Article

Keywords: Pulverized coal flames; Coal combustion modeling; Probability density function method

Corresponding Author: Ms. Xinyu Zhao,

Corresponding Author's Institution: The Pennsylvania State University

First Author: Xinyu Zhao

Order of Authors: Xinyu Zhao; Daniel C Haworth, Ph. D.

Abstract: A transported composition probability density function (PDF) method is developed for pulverized coal combustion. A consistent hybrid Lagrangian particle/Eulerian mesh algorithm is used to solve the modeled PDF transport equation for the gas phase, with finite-rate gas-phase chemistry. The model includes standard k-ε turbulence, gradient transport for scalars, and a Euclidean minimum spanning tree (EMST) mixing model. A separate Lagrangian description is used to solve for the coal particle phase, including particle tracking, coal devolatilization and surface reaction models. Interphase coupling models are developed to handle the interaction between the gas phase and the solid phase. Radiative heat transfer is modeled by a P1 model for a gray absorbing emitting and scattering gas-particle system. Two independent laboratory-scale pulverized coal jet flames ("flame A" and "flame B") studied at the Japanese Central Research Institute of Electric Power are simulated using the new model. For flame A, the baseline model reproduces the measured mean and rms particle axial velocity reasonably well. Some discrepancies are found in particle temperature and gas-phase concentrations, which may in part be due to the uncertainties in the experimental data. Sensitivities of model results to coal-related model variations, turbulence-chemistry interactions, different interphase coupling strategies, and finite-rate chemistry are explored to establish sensitivities and to determine which aspects of the models are most important. The same model is applied to a second flame (flame B), the only change being in parameters related to the different coal composition. It is found that experimental standoff heights cannot be reproduced for three different stoichiometric ratios using a single model. Time scales for chemical reactions, devolatilization and turbulence are extracted and compared, to study the level of turbulence-chemistry-particle interactions in flame A and to test the popular assumption of equilibrium chemistry in coal combustion modeling. Mixture-fraction statistics for flame B are explored to test assumptions that have been proposed for mixture-fraction-based coal models. While the usual assumption of Beta distributions is found to be appropriate, assumptions of statistical independence are not valid.

Suggested Reviewers: Christian Hasse
Professor, TU Bergakademie Freiberg
Christian.Hasse@iec.tu-freiberg.de
Professor Hasse has published paper on similar simulations.

Oliver T Stein
Universität Stuttgart

o.stein@itv.uni-stuttgart.de
The professor has published papers on the same target flames.

Dirk Roekaerts
Delft University of Technology
D.J.E.M.Roekaerts@tudelft.nl
The professor has expertise in similar topic.

Philip J Smith
University of Utah
philip.smith@utah.edu
The professor has published papers on one of the target flames described in this paper.

Transported PDF modeling of pulverized coal jet flames

X. -Y. Zhao, D. C. Haworth

Department of Mechanical and Nuclear Engineering,
The Pennsylvania State University,
University Park, PA 16802

Abstract

A transported composition probability density function (PDF) method is developed for pulverized coal combustion. A consistent hybrid Lagrangian particle/Eulerian mesh algorithm is used to solve the modeled PDF transport equation for the gas phase, with finite-rate gas-phase chemistry. The model includes standard $k-\varepsilon$ turbulence, gradient transport for scalars, and a Euclidean minimum spanning tree (EMST) mixing model. A separate Lagrangian description is used to solve for the coal particle phase, including particle tracking, coal devolatilization and surface reaction models. Interphase coupling models are developed to handle the interaction between the gas phase and the solid phase. Radiative heat transfer is modeled by a $P1$ model for a gray absorbing emitting and scattering gas-particle system. Two independent laboratory-scale pulverized coal jet flames ("flame A" and "flame B") are simulated using the new model. For flame A, the baseline model reproduces the measured mean and rms particle axial velocity reasonably well. Some discrepancies are found in particle temperature and gas-phase concentrations, which may in part be due to the uncertainties in the experimental data. Sensitivities of model results to coal-related model variations, turbulence-chemistry interactions, different interphase coupling strategies, and finite-rate chemistry are explored to establish sensitivities and to determine which aspects of the models are most important. The same model is applied to a second flame (flame B), the only change being in parameters related to the different coal composition. It is found that experimental standoff heights cannot be reproduced for three different stoichiometric ratios using a single model. Time scales for chemical reactions, devolatilization and turbulence are extracted and compared, to study the level of turbulence-chemistry-particle interactions in flame A and to test the

popular assumption of equilibrium chemistry in coal combustion modeling. Mixture-fraction statistics for flame B are explored to test assumptions that have been proposed for mixture-fraction-based coal models. While the usual assumption of Beta distributions is found to be appropriate, assumptions of statistical independence are not valid.

Keywords: Pulverized coal flames; Coal combustion modeling; Probability density function method

1. Introduction

Coal combustion is, and is expected to remain, a major source of electricity generation, especially for countries including the United States and China that have high electricity demand and large coal reserves [1]. Recent research interest on coal focuses on increasing combustion efficiency while decreasing pollutant and greenhouse-gas emissions, such as NOx and CO_2. Among the various possible ways of efficiency enhancement and CO_2 reduction, direct power extraction using magnetohydrodynamics (MHD) combined with high-temperature oxygen-coal combustion has been revisited recently [2]. High-fidelity computational fluid dynamics (CFD) models are desired to help design and optimize the combustion systems, due to the scarcity of experimental data and lack of experience in these high-temperature environments, where furnace temperature can be as high as 3000 K, with high concentrations of radicals, CO_2 and H_2O.

The process of pulverized coal combustion can be divided into four main steps: heating up/water evaporation, devolatilization, volatile gases combustion, and char surface reactions. Accurate property data and physical submodels are required for quantitative predictions [3, 4, 5, 6]; these include the thermodynamic properties of coal components, devolatilization rates and components, surface reaction rates, coal off-gas mixing and combustion, and interactions between particles, turbulence, chemistry and radiation.

Turbulence-chemistry interactions (TCI) is one aspect that has received little attention to date. Turbulence-chemistry interactions can be important in determining the correct mixing level for volatile gases evolved from the particle phase. Under rapid heating conditions, variations in devolatilization and surface-reaction rates due to turbulent fluctuations are another manifestation of turbulence-chemistry interactions. In most of the turbulent coal combustion modeling studies, simple models such as the eddy-breakup (EBU)

model and eddy-dissipation-concept (EDC) model have been used to account for the effect of turbulence-chemistry interactions [6]. These models are not expected to be as accurate as higher-fidelity models, such as the conditional moment closure (CMC) model [7] and transported probability density function (PDF) models [8]. Models that have been designed specifically for turbulent coal combustion can have different limitations; for example, the widely used local equilibrium chemistry assumption cannot capture the effects of finite-rate chemistry (e.g., CO oxidation) [9]. As large-scale computational power has become more widely available, more research efforts have focused on incorporating higher-fidelity models that have been developed for gaseous turbulent flames, into coal combustion modeling [10, 11, 12]. For example, a comprehensive set of coal combustion models, including a transported velocity-composition PDF model for the gas phase, has been established in [11]. One limitation of the method developed in [11] is the adoption of local equilibrium chemistry, which might not be sufficient if the prediction of slowly reacting species such as CO is desired, because CO concentrations can be significantly above equilibrium values in pulverized coal flames [5]. An important aspect of the modeling effort in dual-Lagrangian-particle formulations such as that used in [11] (coal particles and gas-phase notional particles) is the interaction between phases, as represented through modeling of the interphase source terms [10, 11].

The purpose of this research is to develop a comprehensive model for high-temperature pulverized coal combustion, such as that encountered in the combustor for an open-cycle MHD system, with particular emphasis on the turbulence-chemistry interaction models. This is being pursued by coupling a transported composition PDF method with realistic finite-rate gas-phase chemical mechanisms and widely-employed coal submodels. A systematic approach is being pursued for model development. In earlier work, simulations were performed for laboratory syngas-air nonpremixed flames [13] and a high-temperature oxy-natural gas system [14]. There the models were extended towards the thermochemical environments of interest, without the complications of coal particles, and good agreement with experiment was realized. The next step is to add coal particles and coal combustion, and that is the subject of this paper. In the earlier work, a stochastic Lagrangian particle method was used to implement the transported PDF method, including realistic finite-rate chemistry. Here a separate Lagrangian description is adopted for the solid phase (coal particles).

Compared to the mixture-fraction-based models that have been employed

earlier in coal simulations, the use of a detailed composition specification here in terms of species mass fractions and mixture specific enthalpy allows one to handle situations such as multiple inlets with different compositions (e.g., natural gas-coal co-firing) and non-adiabatic systems in a more nature manner. Without additional effort on the gas-phase modeling, it can also accommodate different evolution rates of different coal off-gas components, if the devolatilization model provides information on individual mass evolution rates. And finite-rate chemistry, such as CO oxidation, can also be captured, by properly choosing the gas-phase chemical mechanism.

In this paper, the framework for extending a transported composition PDF method to coal combustion is established first. The reliability of existing PDF submodels (e.g., mixing models) and numerical strategies (e.g., ISAT [15]), is explored, in this complicated new environment. Model results are compared with experimental measurements for two different pulverized coal-air flames. Variations in key models and model parameters are then made to explore the sensitivities. Finally, the high-fidelity model is used to test key assumptions that have been made in simpler mixture-fraction-based models for turbulent coal combustion.

The rest of the paper is organized as follows. In the following section, the target flames are introduced and findings from earlier modeling studies are summarized. In Section 3, the numerical methods and physical models are described. Comparisons with experimental measurements and sensitivities to variations in models are reported in Section 4. Finally, key findings are summarized and next steps are outlined.

2. Pulverized-coal jet flames

A laboratory-scale methane-piloted pulverized-coal jet flame is the first target configuration, and will be referred to as "flame A" (Table 1). The flame was studied experimentally at the Japanese Central Research Institute of Electric Power Industry (CRIEPI) [16]. As a laboratory-scale jet flame, coal particles are injected through a central nozzle, carried by air. The main jet is surrounded by a methane annular jet, which is ignited first, and serves as a pilot to ignite the coal particles. The Reynolds number of the central jet flow is approximately 2,500 based on ambient viscosity, which is transitional rather than fully turbulent. Measurements reported in [16] include axial mean and rms particle velocities, axial mean particle temperature, radial distributions of coal particle size at different axial locations, and mean mole

fractions of O_2, CO_2, CO and N_2. Compared to global parameters such as carbon burnout and ignition delay, these detailed measurements more fully reveal the structure of the jet coal flame. Newland bituminous coal was used in the experiments; the composition of the coal particles and the heating values are listed in Table 2. The injected particle-size distribution is also given in [16]. The boundary conditions for this flame are thus reasonably well defined, compared to other available data sets. Figure 1 shows the geometry of the injector.

Flame A has been the subject of several modeling studies, using both RANS- and LES- based methods [17, 18, 19, 20]. Bermudez et al. [17] used this flame to validate their group combustion models. There volatile gases were assumed to burn infinitely fast on a flame front. A basic assumption of the group combustion model is that no oxygen is left inside the flame zone, while no volatile fuel is present outside the flame. Judging by the experimental oxygen measurements, this assumption might not be valid for this flame. Hashimoto et al. [19] implemented a tabulated devolatilization model (TDP model), which can account for the influence of varying heating rates on the devolatilization rates. Comparisons were made between the TDP model and conventional single-rate and two-rates models. By carefully choosing the model parameters, the conventional models could give results similar to those from the TDP model. However, these parameters are case-dependent and require a priori knowledge of the heating condition of the system, so that the TDP model is more predictive. In [18, 20], three research groups used different LES-based coal combustion codes to explore the same flame, and differences of the results from the different models were used to draw conclusions regarding which aspects of the modeling were most important. It was postulated that a better turbulence-chemistry-interaction model might improve the oxygen prediction along the centerline.

All the available studies showed reasonable agreement with the experimental data in at least some respects. The largest disagreements were seen in the gas-phase concentrations and solid-phase temperature. However, arguments have also been made concerning the reliability of the experimental data, especially for the gas-phase measurements. This point will be discussed further in Section 4.1.1.

It has been observed that flame A is essentially a methane flame with coal particles burning in it [20]. Experimental measurements of the total volatile release and char gasification [17] show that less than half of the volatile matter is burned and a very small amount of char is gasified. Thus, this flame is

dominated by gaseous combustion. To further validate the models, especially the surface reaction model and interphase coupling models, a second pulverized coal jet flame ("flame B") is simulated for which different measurements are available. The details of the experimental setup and coal composition can be found in [21]. Instead of a methane pilot, the coal particles are ignited by the exhaust gas of propane combustion. Available experimental results for flame B include stand-off distance for three different inlet stoichiometric ratios ($sr = 0.14$, $sr = 0.22$, $sr = 0.36$), as well as gas-phase temperature and carbon burnout along the centerline for $sr = 0.22$. Here sr is defined as $sr = \frac{actual\ air\ mass\ from\ inlet}{air\ mass\ that\ is\ required\ to\ completely\ burn\ the\ inlet\ coal}$. It has been shown in [22] that RANS-based models could not capture correctly the highly transient phenomenon of coal ignition that was observed in the experiments. Here, the baseline models used in simulating flame A are applied to simulate flame B, with model parameters adjusted only as necessary to account for the different composition and reactivity of the coal used in the experiment. The purpose of simulating flame B is twofold. First, simulating a second flame using the same models complements the validation of the models, with an emphasis on capturing global characteristics such as stand-off distance and carbon burnout. Second, the statistics of the volatile gas and char gasification gas can be better studied using this flame, since more char is gasified in flame B than in flame A.

The majority of the results and discussion in this paper focus on flame A (Section 4.1). Results for flame B are discussed in Sections 4.2.

3. Simulation methods and models

A consistent hybrid Lagrangian particle/Eulerian mesh method is used to solve a modeled transport equation for the joint PDF of species mass fractions and mixture specific enthalpy in a Reynolds-average formulation for the gas phase. The coupled mean continuity, mean momentum and turbulence model equations are solved using an unstructured finite-volume method with second-order spatial discretizations and first-order time discretization using a PISO-based, time-implicit segregated solver that has been built using elements from OpenFOAM-1.7.1 [23]. The stochastic Lagrangian particle-based gas-phase advection, mixing, and reaction for the PDF method are implemented using a FORTRAN code that is coupled with the OpenFOAM CFD solver. A separate stochastic Lagrangian particle method is used for the dispersed solid phase (coal particles).

3.1. Gas-phase transport and combustion

The Favre-averaged continuity, momentum, species mass fraction and energy (absolute enthalpy) equations for the gas phase can be written as follows:

$$\frac{\partial\langle\rho\rangle}{\partial t}+\frac{\partial\langle\rho\rangle\tilde{u}_i}{\partial x_i}=\langle\rho m_0\rangle=\langle\rho\rangle\tilde{m}_0, \quad (1)$$

$$\frac{\partial\langle\rho\rangle\tilde{u}_i}{\partial t}+\frac{\partial\langle\rho\rangle\tilde{u}_i\tilde{u}_j}{\partial x_j}=-\frac{\partial p}{\partial x_i}-\frac{\partial\langle\rho\rangle\widetilde{u_i''u_j''}}{\partial x_j}+\frac{\partial\langle\tau_{ji}\rangle}{\partial x_j}+\langle\rho\rangle g_i+\langle S_{u_i}\rangle \ (i=1,2,3), \quad (2)$$

$$\frac{\partial\langle\rho\rangle\tilde{Y}_\alpha}{\partial t}+\frac{\partial\langle\rho\rangle\tilde{Y}_\alpha\tilde{u}_i}{\partial x_i}=-\frac{\partial\langle\rho\rangle\widetilde{u_i''Y_\alpha''}}{\partial x_i}-\frac{\partial\langle J_i^\alpha\rangle}{\partial x_i}+\langle\rho\rangle\tilde{S}_\alpha+\langle\rho m_\alpha\rangle \ (\alpha=1,2,...,N_s), \quad (3)$$

$$\frac{\partial\langle\rho\rangle\tilde{h}}{\partial t}+\frac{\partial\langle\rho\rangle\tilde{h}\tilde{u}_i}{\partial x_i}=-\frac{\partial\langle\rho\rangle\widetilde{u_i''h''}}{\partial x_i}-\frac{\partial\langle J_i^h\rangle}{\partial x_i}+\frac{D\langle p\rangle}{Dt}+\Phi-\langle\dot{Q}_{rad,g}\rangle+\langle\rho\dot{h}_0\rangle \ . \quad (4)$$

Here angled brackets denote conventional averages, tildes denote density-weighted (Favre) averages, and double primes denote fluctuations about Favre-averaged values. A Roman subscript denotes a physical-space coordinate ($i=1,2,3$), a Greek subscript denotes one of the N_S chemical species, and summation is implied over a repeated Roman index within a term. $\boldsymbol{u}$ is the velocity vector, τ_{ji} is the viscous stress, and Y_α, $\boldsymbol{J}_\alpha$ and S_α are the mass fraction, molecular flux vector and the chemical source term for species α, respectively. h is the the mixture-specific absolute enthalpy, p is the gas-phase pressure, Φ is the mean viscous dissipation rate of kinetic energy to heat, and $\dot{Q}_{rad,g}$ is the volume rate of heating due to radiation (absorption minus emission) for the gas phase. $\langle\rho m_0\rangle$, $\langle S_{u_i}\rangle$, $\langle\rho m_\alpha\rangle$, and $\langle\rho\dot{h}_0\rangle$ are the mean source terms resulting from coal particle motion and reactions, which are collected in a particle-source-in-cell (PSIC) [24] manner, where each term is calculated as the sum of the contributions over all of the coal particles in each computational cell. Turbulence is accounted for using a standard $k-\varepsilon$ model. Radiation is modeled using a $P1$ method for a gray, absorbing, emitting and scattering gas medium containing absorbing, emitting and isotropically scattering solid particles. The transport equation for the mean incident radiation $\langle G\rangle$ is

$$\nabla\cdot(\Gamma\nabla\langle G\rangle)-(a+a_p)\langle G\rangle+4\pi(a\frac{\sigma\langle T\rangle^4}{\pi}+\langle E_p\rangle)=0, \quad (5)$$

where a is the absorption coefficient for the gray gas and E_p and a_p are the equivalent emission of the coal parcels and the equivalent absorption coef-

ficient of the coal parcels, respectively. σ is the StefanBoltzmann constant. For a computational cell containing N parcels with P_i particles per parcel, these are defined as:

$$\langle E_p \rangle = \sum_{i=1}^{N} \epsilon_{p,i} A_{p,i} \frac{P_i \sigma T_{p,i}^4}{\pi V_c}, \tag{6}$$

$$a_p = \sum_{i=1}^{N} \epsilon_{p,i} \frac{P_i A_{p,i}}{\pi V_c}, \tag{7}$$

$$\Gamma = \frac{1}{3(a + a_p + \sigma_p)}, \tag{8}$$

where $\epsilon_{p,i}$ is the emittance for parcel i, σ_p is the equivalent scattering coefficient calculated as $\sigma_p = \sum_{i=1}^{N} (1-\epsilon_{p,i})(1-f_{p,i}) \frac{P_i A_{p,i}}{\pi V_c}$, and $f_{p,i}$ is the scattering factor associated with the n^{th} parcel. These properties are used to solve for the mean incident radiation $\langle G \rangle$. Once the field of $\langle G \rangle$ is obtained, the mean radiation source term in the mean enthalpy equation (Eq. (4)) is obtained as,

$$\langle \dot{Q}_{rad,g} \rangle = a \langle G \rangle - 4a\sigma \langle T \rangle^4.$$

A composition transported PDF method has been adopted here to describe the gas-phase combustion. The N_S+1 composition variables are taken to be the mass fractions of the N_S species $\boldsymbol{Y}$ in the chemical mechanism, plus the mixture-specific absolute enthalpy h (sum of sensible and formation enthalpies). These are sufficient to determine any thermodynamic or transport properties that are needed. The sample-space vector corresponding to the N_S+1 composition variables $(\boldsymbol{Y} + h)$ is denoted as $\boldsymbol{\psi}$. Then the PDF transport equation, expressed as an equation for the composition mass density function $\mathcal{F} = \mathcal{F}(\boldsymbol{\psi}; \boldsymbol{x}, t)$, can be written as,

$$\begin{aligned} &\frac{\partial \mathcal{F}}{\partial t} + \frac{\partial}{\partial x_i}[\tilde{u}_i \mathcal{F}] + \frac{\partial}{\partial \psi_\alpha}[S_\alpha(\boldsymbol{\psi}) \mathcal{F}] \\ &= -\frac{\partial}{\partial x_i}[\langle u_i'' | \boldsymbol{\psi} \rangle \mathcal{F}] + \frac{\partial}{\partial \psi_\alpha}[\langle \rho^{-1}(\boldsymbol{\psi}) \frac{\partial J_i^\alpha}{\partial x_i} | \boldsymbol{\psi} \rangle \mathcal{F}] - \delta_{\alpha h} \frac{\partial}{\partial \psi_\alpha}[\langle \rho^{-1}(\boldsymbol{\psi}) \dot{Q}_{rad,g} | \boldsymbol{\psi} \rangle \mathcal{F}] \\ &\quad + \mathcal{F} \langle m_0 | \boldsymbol{\psi} \rangle - \frac{\partial}{\partial \psi_\alpha}[\langle m_\alpha - m_0 \psi_\alpha | \boldsymbol{\psi} \rangle \mathcal{F}] - \delta_{\alpha h} \frac{\partial}{\partial \psi_\alpha}[\langle \dot{h}_0 - m_0 h | \boldsymbol{\psi} \rangle \mathcal{F}] \ . \end{aligned} \tag{9}$$

Here $\delta_{\alpha h}$ denotes the Kronecker delta function ($\delta_{\alpha h} = 1$ for $\alpha = N_S + 1$ corresponding to enthalpy h; $\delta_{\alpha h} = 0$ otherwise) and the notation $\langle A | B \rangle$

denotes the conditional mean of event A given that event B occurs. The left-hand-side terms are in closed forms, while the right-hand-side terms require modeling. The first three terms on the right-hand side represent turbulent transport, molecular mixing, and net radiative heat transfer for the gas-phase [14]. The last three terms represent the coupling between the solid phase and the gas phase, which is discussed in Section 3.3. Equation 9 effectively replaces Eqs. (3) and (4), since $\tilde{Y}_\alpha$ and $\tilde{h}$ can be determined from $\mathcal{F}$.

With the gradient transport model for transport by turbulent velocity fluctuations, a notional particle system that is equivalent to Eq. (9) is:

$$dx_i^* = \tilde{u}_i^* dt + (\langle\rho\rangle^{-1}\frac{\partial\Gamma_{T\phi}}{\partial x_i})^* dt + (2\langle\rho\rangle^{-1}\Gamma_{T\phi})^{*1/2} dW_i, \tag{10}$$

$$\begin{aligned} d\phi_\alpha^* = S_\alpha(\boldsymbol{\phi}^*)dt + \theta_{\alpha,mix}^* dt - \delta_{\alpha h}\dot{Q}_{rad,g}(\boldsymbol{\phi}^*)dt \\ +(m_0(c_\alpha - \phi_\alpha^*))|_{\boldsymbol{x}^*(t)}dt + \delta_{\alpha h}(\dot{h}_0 - m_0 h^*))|_{\boldsymbol{x}^*(t)}dt \ , \end{aligned} \tag{11}$$

where the superscript * refers to a notional gas-phase particle. Here $\boldsymbol{W}$ is an isotropic vector Wiener process. In a numerical implementation, dW_i normally is discretised (approximated) as $\triangle W_i = W_i(t+\triangle t) - W_i(t) = \eta_i \triangle t^{1/2}$, where $\boldsymbol{\eta}$ is a vector of three independent standardised Gaussian (zero mean, unit variance) random variables and $\triangle t$ is the computational time step. The apparent turbulent diffusivity $\Gamma_{T\phi}$ is given by $\Gamma_{T\phi} = C_\mu\langle\rho\rangle\sigma_\phi{}^{-1}k^2/\varepsilon$ for a $k-\varepsilon$ model, where σ_ϕ is the apparent turbulent Schmidt number. $S_\alpha(\boldsymbol{\phi}^*)$ is obtained from the gas-phase chemical mechanism, without further approximation. For simplicity, $\dot{Q}_{rad,g}(\boldsymbol{\phi}^*)$ is modeled as $\langle\dot{Q}_{rad,g}\rangle$, neglecting the influence of turbulent fluctuations on radiative transfer ("turbulence-radiation interactions") [14]. The molecular transport ("mixing") term, $\theta_{\alpha,mix}^*$, is modeled using either the Euclidean minimum spanning tree (EMST) model [25] or a modified Curl's model [26]. Here c_α denotes the local mass fraction of species α that comes from the solid phase, which is a constant for a given computational cell at each time step. The nonzero components of c_α include the composition of the volatile gases in the coal, plus O_2 and CO_2 for the surface reactions. The only terms that remain to be modeled are m_0 and $\dot{h}_0$, which correspond to the coupling between the solid phase and the gas phase. These will be discussed in detail in Section 3.3.

3.2. Solid-phase transport and combustion

A separate stochastic Lagrangian description is used to describe the solid-phase particles. To distinguish the two sets of Lagrangian particles that are

used, the gas-phase particles henceforth will be referred to as "notional particles", and the dispersed coal-phase particles as "coal parcels". The underlying probability density functions of the state of the two sets of Lagrangian systems are assumed to be statistically independent, and the two phases are coupled by a particle-source-in-cell [24] method, which is intended for a dispersed-phase system that does not account for particle-particle interactions. Coal particles are grouped into parcels identified by their initial size distribution, and each parcel moves along its own trajectory. The shape of the coal particles is assumed to be spherical, and the mass m_p of a single particle with diameter d_p is calculated as $m_p = \rho_p \pi d_p^3/6$. The trajectory of each parcel is governed by the following equations:

$$\frac{d\boldsymbol{x_p}}{dt} = \boldsymbol{u_p}, \tag{12}$$

$$\frac{d\boldsymbol{u_p}}{dt} = -\frac{\boldsymbol{u_p} - \boldsymbol{u}}{\tau_D} + (1 - \frac{\rho}{\rho_p})\boldsymbol{g} + \boldsymbol{f}_{other}, \tag{13}$$

where $\boldsymbol{x_p}$ and $\boldsymbol{u_p}$ are the instantaneous parcel position and velocity, respectively. The first term on the right-hand side of Eq. (13) represents the drag force, the second term accounts for gravity and buoyancy, and the last term includes all other effects such as Magnus force, Saffman force, particle thermophoresis, electrophoresis and photophoresis, etc., which are expected to be negligible in the context of pulverized coal combustion [27]. Here τ_D is the momentum relaxation time of the particle, which determines the rate at which the parcel velocity $\boldsymbol{u_p}$ relaxes to the instantaneous surrounding gas velocity $\boldsymbol{u}$. In the limit of Stokes flow (where the particle Reynolds number $Re_d \equiv \frac{\rho \|\mathbf{u}-\mathbf{u_p}\| d_p}{\mu}$ approaches 0),

$$\tau_D^{st} = \frac{\rho d_p^2}{18\mu}, \tag{14}$$

and τ_D is related to τ_D^{st} through the drag coefficient C_D:

$$\tau_D = \tau_D^{st} \frac{24}{Re_d C_D}, \tag{15}$$

where C_D is modeled as [27]

$$C_D = \begin{cases} \frac{24}{Re_d}(1 + \frac{1}{6}{Re_d}^{2/3}) \text{ for } Re_d \leq 1000 \\ 0.424 \text{ for } Re_d > 1000. \end{cases}$$

For a reacting coal particle, the drag coefficient tends to be reduced due to mass ejection during the rapid devolatilization processes. Following the suggestion of [3], the following correlation is used to calculate the reduced drag coefficient:

$$C_{D,m} = C_D exp(-\phi_m),$$

where ϕ_m is defined as $\phi_m = 2\dot{m}_{vol} c_{pm}/(k_m d_p)$. The subscript m denotes that the properties are evaluated at the arithmetic mean of the surface and surrounding gas-phase temperature. Here $\dot{m}_{vol}$ is the devolatilization mass transfer rate, which will be discussed later in this section, c_{pm} is the gas-phase specific heat, d_p is the diameter of the coal particle, and k_m is thermal conductivity of the gas phase.

Parcel dispersion due to turbulence is usually modeled using stochastic models. In this study, a discrete random walk model is used to describe the effect of gas-phase turbulent fluctuations on parcel movements. The effect of turbulent dispersion is expressed by modeling the instantaneous gas-phase velocity, $\boldsymbol{u}$. In the context of standard $k-\varepsilon$ turbulence model, $\boldsymbol{u}$ is computed as

$$\boldsymbol{u} = \tilde{\boldsymbol{u}} + (\sigma_1\sqrt{\frac{2k}{3}}, \sigma_2\sqrt{\frac{2k}{3}}, \sigma_3\sqrt{\frac{2k}{3}}),$$

where σ_i are three normally distributed independent random variables with zero mean and unit variance. Once the instantaneous gas-phase velocity is obtained, a time scale is required to calculate the interaction time between the parcels and the turbulent eddies. Two possible choices are the eddy turnover time τ_{eddy}, or the parcel crossover time τ_{cross}, as defined in Eq. (16) and Eq. (17), respectively:

$$\tau_{eddy} = k/\varepsilon, \tag{16}$$

$$\tau_{cross} = l_e/ \parallel \boldsymbol{u_p} - \boldsymbol{u} \parallel, \tag{17}$$

where the length scale of the eddy is calculated as $l_e = C_\mu k^{1.5}/\varepsilon$. The interaction time then is chosen as the minimum of τ_{eddy} and τ_{cross}. The model presented here is slightly different than what was originally proposed in [28], in terms of the definitions of the two time scales. A preliminary study has been done to compare results for nonreacting particle-laden flow with the model employed in this study and the model proposed in [28], and negligible differences have been found in the context of axisymmetric RANS simulations with $k-\varepsilon$ turbulence models.

The quantity $\dot{m}_{vol}$ is obtained through devolatilization models. A single-rate devolatilization model and a two-rates devolatilization model [29] have been tested in this work. The single-rate model is described by Eq. (18):

$$\begin{aligned} \dot{m}_{vol} &= k_v(m^*_{vol,0} - m_{vol}), \\ k_v &= A_v exp(-E_v/RT_p), \\ m^*_{vol,0} &= Q m_{vol,0}, \end{aligned} \tag{18}$$

where $m_{vol,0}$ is the amount of volatile predicted from the proximate analysis. It has been shown that the amount of volatile released during rapid heating (heating rate above 10^4 K/s) [30] is greater than what is given by the proximate analysis, and this is quantified by a factor Q. The values of Q, k_v, and E_v are assigned according to [19], in which the results of a chemical percolation devolatilization model (CPD) analysis of the same coal and heating rate is provided. A two-rates model, which has two parallel reaction paths for low- and high-temperature ranges [29], also has been tested in this study. The two-rates model can be written as follows:

$$\begin{aligned} \dot{m}_{vol} &= k_v(m^*_{vol,0} - m_{vol}), \\ k_v &= \alpha_1 A_{v1} exp(-E_{v1}/RT_p) + \alpha_2 A_{v2} exp(-E_{v2}/RT_p). \end{aligned} \tag{19}$$

The original model parameters of Kobayashi [29] are used in this study, which has been found to be appropriate for the target flames [19].

Devolatilization and surface reaction are assumed to occur sequentially, and the global reaction of $C + O_2 = CO_2$ is considered as the heterogeneous reaction. A diffusion-kinetic-controlled surface reaction model [31] is used to describe the reaction rate:

$$\begin{aligned} \frac{dm_{char}}{dt} &= -(\frac{K_c K_d}{K_c + K_d}) p_{O_2} \pi d_p^2, \\ K_d &= 5.06 \times 10^{-7} \times d_p^{-1} ((T_p + T_g)/2)^{0.75}, \\ K_c &= A_c exp(-E_c/RT_p). \end{aligned} \tag{20}$$

The surface reaction described in Eq. (20) is a first-order reaction. A different model [32] also has been tested that can accommodate varying reaction orders, which might be important for conditions with elevated oxygen content. Equations. (18), (19) and (20) describe the mass transfer rate between the gas phase and the solid phase. The inter-phase heat transfer rate

is described by Eq. (21):

$$m_p \frac{c_{p,p} dT_p}{dt} = -A_s h_{conv}(T_p - T_g) - A_s \epsilon_p (\sigma T_p^4 - \frac{\langle G \rangle}{4}) + \triangle h_{lat} \dot{m}_{p,water} + \triangle h_{devol} \dot{m}_{p,vol} + \triangle h_{char} \dot{m}_{p,char}, \quad (21)$$

where A_s is the surface area of a spherical particle, h_{conv} is the convective heat-transfer coefficient defined as $h_{conv} = Nuk_m/d_p$, ϵ_p is the emittance of the parcel, and $\langle G \rangle$ is the mean incident radiation evaluated at the particle position. The Nusselt number for a coal parcel is given by the Ranz-Marshall model as $Nu_0 = 2.0 + 0.6 Re_p^{\frac{1}{2}} Pr^{\frac{1}{3}}$. Similar to what was done for the drag-model correction, the effect of the emitted gas on heat transfer is also considered through the introduction of blowing factor B, which is defined as $B = \frac{\dot{m}_{p,vol} c_{p,m}}{2\pi d_p k_m}$. The modified Nusselt number due to blowing is $Nu = Nu_0 exp(-0.6B)$ for Re_d up to 400, and $Nu = Nu_0 \frac{B}{exp(B)-1}$ for $Re_d = 0$.

The specific heat $c_{p,p}$ depends on the coal parcel temperature and composition. For a coal particle with a composition $(Y_{ash}, Y_{char}, Y_{volatile})$, $c_{p,p}$ is defined as

$$c_{p,p} = Y_{volatile} c_{p,vol}(T_p) + Y_{ash} c_{p,ash} + Y_{char} c_{p,char}.$$

In the current model, both $c_{p,ash}$ and $c_{p,char}$ are assumed to be constant, and independent of temperature. The effect of c_p will be discussed later, in Section 4.1, and $c_{p,volatile}$ is estimated according to the composition of the gas-phase volatile species at the gas-phase temperature surrounding the particle.

It is assumed that 30% of the surface reaction heat is retained in the coal particle, and 70% is released into the gas phase [31]. This assumption is also examined in Section 4.1. A Rosin-Rammler distribution is used to describe the initial size distribution of the parcels in the coal injection models, and the model parameters are selected based on the experimental measurement of coal-particle-size distribution [17]. The diameter of the coal particles is assumed to be constant during the reaction process. It has been shown that there can be a swelling effect during the devolatilization process, which can make the particle diameter grow to as big as twice the initial value. The swelling effect has been found to be more influential on larger particles, while

it does not change the small-particle statistics significantly [20]. Thus, it is not included in this study.

3.3. Coupling between gas and solid phases

As mentioned in Section 3.2, the solid phase is coupled with the gas phase by a particle-source-in-cell method. Since a Lagrangian representation is also used for the gas phase in the transported PDF method, the coal parcel inter-phase source terms collected in each computational cell need to be re-distributed to the gas-phase notional particles in that cell. Several coupling approaches have been proposed in the context of liquid spray-PDF coupling [33] to account for vaporization. However, the case of coal is more complicated. Three different processes in coal combustion involve interaction with the gas phase: water evaporation, devolatilization, and surface reactions. Evaporation and devolatilization are endothermic with respect to the coal particle (heat transfer from gas to solid phase) and increase the mass in the gas phase (condensation is not considered). Surface reactions can be either endothermic or exothermic, and can either consume or produce individual gas-phase species. The three processes are assumed to take place sequentially. However, in each computational cell, some coal parcels might be undergoing devolatilization, while others are active in surface reactions, depending on the burning rate of each coal parcel (which is influenced by diameter, temperature, etc.). Thus, the source terms for mass and specific enthalpy can be either positive or negative, and mass sources/sinks exist for multiple chemical species (compared to one species, fuel, for most spray applications). Great care is needed in handling the source-term distribution, to avoid having any of the notional gas-phase particle properties take on unphysical values.

The m_0 term in Eqs. (9) and (11) is modeled at the particle level as $S_0(\boldsymbol{\phi}^*(t))$: a function of the local instantaneous particle composition $\boldsymbol{\phi}^*(t)$. For a computational cell with N_p notional particles, a consistency requirement for mass transfer between the solid and gas phases is:

$$\frac{\sum_{i=1}^{N_p} m_p^{(i)} S_0^{(i)}}{\sum_{i=1}^{N_p} m_p^{(i)}} = \frac{\langle \rho m_0 \rangle}{\langle \rho \rangle}, \tag{22}$$

where the coal models provide the total mass transferred from the solid phase to the gas phase: $\langle S_m \rangle_c = \langle \rho m_0 \rangle \times \Delta t \times V_c$. V_c is the computational cell volume and Δt is the computational time step. Similarly, the total energy transferred from the solid phase to the gas phase is $\langle S_h \rangle_c = \langle \rho \dot{h}_0 \rangle \times \Delta t \times V_c$.

Three models are proposed here for $S_0(\boldsymbol{\phi}^*(t))$. Model 1 follows what has been widely used in PDF/spray modeling studies [34], where the mass and energy are distributed homogeneously over particles in the cell. The mass assigned to the i_{th} particle in a cell with N_p particles, is then,

$$S_0^{(i)} = \frac{\langle S_m \rangle_c m_p^{(i)}}{\sum_{i=1}^{N_p} m_p^{(i)}} \times \frac{1}{m_p^{(i)}} \times \frac{1}{\Delta t} = \frac{\langle \rho m_0 \rangle}{\frac{\sum_{i=1}^{N_p} m_p^{(i)}}{V_c}} = \frac{\langle \rho m_0 \rangle}{\langle \rho \rangle}. \tag{23}$$

The consistency condition (Eq. (22)) is satisfied automatically, since the source term is independent of the particle composition.

In Model 2, the mass assigned to each particle is biased, based on particle temperature. This model is proposed based on the argument that each notional particle represents a realization of the turbulent flow field, and higher particle temperature implies faster evaporation, devolatilization and surface reaction. Model 2 can be expressed as,

$$S_0^{(i)} = \frac{\langle S_m \rangle_c m_p^{(i)} T_p^{(i)}}{\sum_{i=1}^{N_p} m_p^{(i)} T_p^{(i)}} \times \frac{1}{m_p^{(i)}} \times \frac{1}{\Delta t} = \frac{\langle \rho m_0 \rangle T_p^{(i)}}{\langle \rho \rangle T_c}, \tag{24}$$

where T_c is the cell Favre-averaged mean temperature, which is calculated as the mass-weighted average over the particles in the cell: $T_c = \frac{\sum_{i=1}^{N_p} m_p^{(i)} T_p^{(i)}}{\sum_{i=1}^{N_p} m_p^{(i)}}$.

Model 3 is based on arguments similar to those for Model 2. However, instead of using the particle temperature as the weight factor, a reactivity-weighted formulation is used:

$$S_0^{(i)} = \frac{\langle S_m \rangle_c m_p^{(i)} exp(-C/t_p^{(i)})}{\sum_{i=1}^{N_p} m_p^{(i)} exp(-C/t_p^{(i)})} \times \frac{1}{m_p^{(i)}} \times \frac{1}{\Delta t} = \frac{\langle \rho m_0 \rangle exp(-C/t_p^{(i)})}{\langle \rho \rangle \frac{\sum_{i=1}^{N_p} m_p^{(i)} exp(-C/t_p^{(i)})}{\sum_{i=1}^{N_p} m_p^{(i)}}}, \tag{25}$$

where C is an activation temperature, which is taken to be a constant. Here $C = 5,000$ K has been used, which is close to the value for carbon surface reactions in the coal models. Model 2 and Model 3 also satisfy the consistency requirement (Eq. (22)).

The enthalpy inter-phase source term $S_h^{(i)}$ is expressed in a form similar

to the mass source term for each model:

$$S_h^{(i)} = \frac{\langle \rho \dot{h}_0 \rangle}{\langle \rho \rangle} \text{ (Model 1)}, \tag{26}$$

$$S_h^{(i)} = \frac{\langle \rho \dot{h}_0 \rangle T_p^{(i)}}{\langle \rho \rangle T_c} \text{ (Model 2)}, \tag{27}$$

$$S_h^{(i)} = \frac{\langle \rho \dot{h}_0 \rangle exp(-C/T_p^{(i)})}{\langle \rho \rangle \frac{\sum_{i=1}^{N_p} m_p^{(i)} exp(-C/T_p^{(i)})}{\sum_{i=1}^{N_p} m_p^{(i)}}} \text{ (Model 3)}. \tag{28}$$

Finally, the mass of each particle evolves as

$$\frac{dm_p^*}{dt} = S_0^* m_p^*. \tag{29}$$

Results obtained from the three models are compared in Section 4.1.4.

3.4. Thermochemical properties and gas-phase reactions

The gas phase is considered to be a reacting ideal-gas mixture. Two different methane-air mechanisms have been used: GRI-Mech 2.11 [35], and a 31-species mechanism [36]. It has been found that the kinetics of the volatile matter are similar to those of lower-molecular-weight hydrocarbon gases, such as CH_4 and CO [37]. Moreover, in the case of flame A, a methane pilot is used. Therefore, it is expected that methane-based mechanisms should be appropriate, at least for flame A. The 31-species mechanism was chosen because it has a relatively small number of species, but it includes key species up to C_2 (C_2H_4 and C_2H_2), which are expected to be important when the volatile matter includes C_2 species. In a preliminary test, GRI-Mech 2.11 and the 31-species mechanism were found to give similar results for computed radial profiles of mean temperature and major species for Sandia flame D [38]. The use of a detailed mechanism here can provide additional insight into the flame structure. For example, the OH mass fraction distribution contour can be compared (qualitatively) with the OH PLIF measurement. Compared to highly reduced one-step or two-steps mechanisms, the use of detailed mechanisms increases the computational cost. Here ISAT [15] is used to accelerate chemistry calculations. ISAT has been shown to speed up calculations by a factor of 10 to 100 with respect to direct integration of the chemical source terms, with negligible loss in accuracy, for statistically stationary nonpremixed gaseous jet flames [13, 14].

An alternative treatment that has been used often in coal combustion modeling is to assume infinitely fast (equilibrium) chemistry [37, 39]. This should be a valid approximation when the rates of devolatilization and surface reaction are relatively small compared to those of the gas-phase chemistry. Results from finite-rate chemistry and equilibrium chemistry models are compared in Section 4.1.5, to explore this issue.

3.5. Computational mesh, initial conditions and boundary conditions

Simulations are performed for a two-dimensional (axisymmetric) domain for both flames, for computational expediency. For flame A, the computational domain is a 10-degree wedge with a single finite-volume cell in the azimuthal direction. The domain extends from the jet nozzle exit ($y = 0$) to $y = 0.21$ m in the streamwise direction, and from the jet centerline ($r = 0$) to the acrylic duct wall ($r = 0.03$ m) in the radial direction. An unstructured computational mesh of 9,660 finite-volume cells is used for the baseline model. A maximum difference of 5% in the axial profiles of mean temperature and compositions was found between the baseline model mesh and a refined mesh of 21,735 cells for a gas-phase simulation. A parabolic inlet velocity profile is specified for the jet mean velocity, based on the experimental measurements (Table 3), because the Reynolds number based on the central fuel jet is relatively low ($Re = 2,500$). Top-hat inlet mean velocity and composition profiles are specified for the annular jet and the coflow. The inlet values of k and ε are specified in a manner that corresponds to a turbulence intensity of 10% (estimated from the measured axial mean and rms velocities along the centerline for the coal particles), and a turbulence integral length scale that is 25% of the jet diameter or annulus width. At the outlet, a fixed pressure of one atmosphere is specified and zero-gradient conditions are used for all variables. Zero-gradient conditions also are applied at the outer radial boundary for all variables, and symmetry conditions are applied on the two azimuthal faces. The inlet temperature for the gas and the coal are set to be 300 K.

The coal composition is obtained from the proximate and ultimate analysis. The main elemental components of the dry-ash-free coal are carbon (C), hydrogen (H), nitrogen (N), sulfur (S) and oxygen (O). Sulfur is not considered in the present calculations; the measured amount of sulfur is added to the nitrogen content. The elemental components are distributed among volatile matter, ash, and fixed carbon, according to the proximate analysis. It is assumed that fixed carbon consists solely of carbon (C). Thus,

hydrogen, nitrogen and oxygen are only present in the volatile matter. The volatile elemental composition is calculated based on the proximate and ultimate analysis (Table 2) and the assumptions above. It is also assumed that the volatile matter decomposes to small molecules (C_2H_4, CO, H_2O and N_2) instantaneously. These small molecules then evolve in the gas phase, and react chemically according to the specific gas-phase chemical mechanism. The lower heating value of the volatiles is calculated as:

$$LHV_{vol} = \frac{LHV_{coal} - (1 - Y_{vol}^{daf}) LHV_{char}}{Y_{vol}^{daf}}.$$

Here Y_{vol}^{daf} denotes the mass fraction of volatiles in dry-ash-free coal. The heating values of the prescribed set of small molecules (C_2H_4, CO, H_2O and N_2) can also be calculated and denoted as LHV_{gas}. The difference between LHV_{vol} and LHV_{gas} is minimized by carefully choosing the composition of small molecules. Possible choices for specifying the small molecules can be found in [3, 40]. For the Rosin-Rammler distribution, the mean diameter of the injected coal particles' size distribution is calculated to be 33 μm, and the spread parameter is calculated to be 4.02.

A 10-degree wedge with 15,000 cells has been used to simulate flame B, and similar boundary-condition specification and coal model parameter specification to that for flame A have been used, with values taken from [22].

Results obtained using ISAT have been compared with results calculated using direct integration of the chemical source terms. With a global ISAT error tolerance of 10^{-3}, the maximum differences in gas-phase computed mean temperature and composition between the two are approximately 5%, while the overall simulation time with ISAT is approximately a factor of 50 lower (using four cores) for the baseline flame A model.

4. Results and Discussion

Results for flame A and flame B are presented in subsections 4.1 and 4.2, respectively. Parametric variations in model parameters are explored for flame A. For flame B, mixture fraction statistics that are relevant for simpler models are extracted and discussed.

4.1. Flame A

Results are first presented and discussed with the baseline models for flame A (Table 3). Effects of coal-related model variations are then discussed.

In the last three subsections, the effects of turbulence-chemistry interactions, the effects of different coupling models, and the effects of finite-rate chemistry are explored, in turn.

4.1.1. Baseline model results

A summary of the baseline model is provided in Table 3. The choice of baseline model parameters was determined as follows. A nonreacting case was considered first. There two independent sets of laser measurement were made, and the reported axial measured rms particle velocity profiles were quite consistent with one another. Thus, the velocity data are expected to be relatively reliable. Based on the nonreacting velocity data, the value of $C_{\varepsilon 1}$ is set to be 1.6, higher than the standard value of $C_{\varepsilon 1} = 1.44$. This is consistent with practice in other modeling studies of round jets [41]. Computed mean and rms particle velocity profiles are compared with experiment for the nonreacting case in Fig. 2. Satisfactory agreement with experiment is found for the mean particle velocity. The rms particle velocities are underpredicted at all locations. This might be a limitation of a RANS-based model for this transitional-regime flow, and/or a deficiency of the turbulent dispersion model [42].

It has been shown that the devolatilization model is especially important for coal combustion prediction [19, 43]. Here, the parameters for devolatilization and surface reaction in the baseline model have been taken chosen from the literature [19], and the resulting computed centerline mean profiles are compared with experiment in Fig. 3. The mean particle velocity is overpredicted, which might result from over-prediction of temperature or total mass transfer from the solid phase to the gas phase. The computed mean particle temperature profile differs significantly from the measured profile, and this is similar to what has been reported in earlier modeling studies [18, 20]. As explained in [16], the measured mean temperature should be interpreted as a weighted average of the gas temperature and particle temperature over a relatively large spatial region, because of the measurement technique (two-color pyrometry) that was used in the experiments. Franchetti et al. [18] suggested that it might be more appropriate to compare a weighted particle temperature from the simulation with the experimental profile; they proposed a weight factor proportional to the fourth power of the particle temperature: $T_{weighted} = \sum_{j=1}^{N} T_{p,j}(T_{p,j}^4) / \sum_{j=1}^{N}(T_{p,j}^4)$. Here N denotes the total number of coal parcels in the computational domain at a given axial location. The weighted particle-temperature profile from the baseline model also is shown

in Fig. 3. The weighted temperature profile agrees much better with the experimental data, and further improvement can be achieved with conditional sampling to better correspond to the experimental technique [18].

Moving to the comparisons of gas-phase species in Fig. 3, a first observation is that O_2 is consumed too rapidly along the axis in the model. Similar underprediction of O_2 has been observed in earlier modeling studies [18, 20], where poor mixing and fast chemistry resulting from the use of the eddy-breakup (EBU) model were considered as possible reasons. Here, with the transported composition PDF model and finite-rate chemistry, the consumption of O_2 along the centerline is postponed compared to results from other models [18, 20], but still the O_2 is consumed faster than what the experiment indicates. The choice of devolatilization model can also greatly influence the consumption rate of O_2 [19], and this is discussed later in Section 4.1.2. Experimental uncertainties also may contribute to the discrepancy. For example, it has been suggested that the air mass flow rate from the main jet should be increased by 0.27×10^{-4} m^3/s (normal) to better represent the actual experimental condition [19]. It has also been suggested that water vapor should be added to the calculated N_2 before comparing to the reported N_2 measurement, since the constant N_2 mole fraction reported in the experiment appears to be inconsistent. Furthermore, CO is greatly over-predicted, while the level of CO_2 agrees well with the experimental data. The reason may be that more fuel (volatile matter + coal) has entered into the gas-phase due to improper devolatilization rate, which is implied by the results summarized in Table 4. Table 4 shows the overall computed weight percentage of coal undergoing devolatilization, and the percentage of coal undergoing surface reactions, compared with experimental measurements. The total released volatile gases are slightly over-predicted, and the overall char burnout is underpredicted. The underprediction might be attributed to the sequential occurrence assumption that is used in the baseline model. Under this assumption, surface reaction begins to take place only when the volatile matter has dropped below 0.1%. An alternative model would be to assume that the surface reaction and devolatilization take place simultaneously. The competition between surface reaction and devolatilization then are accommodated by the different reaction rates and the availability of oxygen. The performance of this alternative model will be discussed in the following subsection.

In the remainder of this paper, the focus will be on the differences between results from different model configurations, towards developing insight for

model development, rather than on absolute quantitative agreement with experiment.

4.1.2. Variations in coal submodels

Significant discrepancies between model and experiment have been found for the baseline model. It is emphasized that the differences are smaller compared to what has been reported in earlier modeling studies in most cases, even from LES-based models. Variations in key coal submodels are explored first (Table 5). For convenience, differences between models are quantified by four metrics (Table 6): the maximum computed gas-phase mean temperature along the centerline, the position where oxygen is completely depleted along the centerline, the total released volatile mass fraction, and the total gasified char mass fraction. The first two quantify changes along the centerline, where most of the experimental data are available. The last two are global quantities, because centerline values alone cannot provide a complete picture. This parametric study has been performed without the PDF method, to save computational time. This is sufficient for comparative purposes. Instead, a well-stirred-reactor (WSR) model is used for gas-phase chemistry, where cell-mean values are used to compute reaction rates, rather than particle values (Case 1 in Table 5). The devolatilization model (Case 2) has the most dramatic influence on the results; this is consistent with the findings in [19]. The specific heat used in Case 1 and in the baseline model is a typical value for ash at ambient temperature, while the specific heat used in Case 3 is estimated at 1000 K for both ash and carbon. With increasing temperature, the specific heat of coal particles increases [44]. Increasing heat capacity decreases the peak temperature, and delays the consumption of oxygen. That is a result of the slower temperature increase, which results in a slower rate of devolatilization. The assumption of total retention of char combustion energy (Case 4) does not have a significant impact on the results; this is mainly because the extent of surface reaction is very small in this flame. Case 5 shows an improvement in the prediction of char gasification, due to the assumption of concurrent devolatilization and surface reaction. Although they are frequently assumed to occur sequentially in models, devolatilization and surface reaction may in fact occur simultaneously, and better physical understanding is required to improve the modeling. Case 6 assumes a different composition of the volatiles, where the difference between the predicted volatile heating value and the actual volatile heating value is almost 20%, while the elemental analysis matches with the proximate analysis. In this

case, oxygen is not consumed as rapidly along the centerline. A further examination of Case 6 reveals that the flame is basically heated by the pilot, and there are essentially no coal reaction zones (OH mass fraction ≈ 0). It is important to match the heating value by choosing the proper composition of volatile matter, in the current modeling framework.

From the discussions above, it can be seen that the results from the baseline models can be changed with changes to the coal models, especially the devolatilization model. However, no definitive conclusions can be drawn regarding which model is "better", based on flame A data alone.

The role of turbulence-chemistry interactions is discussed next.

4.1.3. Turbulence-chemistry interactions

Figure 4 compares results obtained from the baseline PDF model and a well-stirred-reactor model for gas-phase chemistry. Differences between results from WSR and PDF models are an indication of the extent to which turbulent fluctuations in composition and temperature, are, or not, important. Compared to WSR model, temperature is predicted to be higher from the PDF model while gas-phase concentrations are predicted to be close to one another, and PDF model results are somewhat closer to experimental measurement in terms of temperature prediction. This suggests that turbulence-chemistry interactions may be important in this flame.

Computed turbulent flame structures from the two models also show differences. Figure 5 shows a broader reaction zone (OH mass fraction contour) for the PDF model, and the PDF results more closely resemble the OH PLIF measurements in [16] (not shown) in the way OH is distributed, compared to the WSR model.

It has been seen in previous PDF studies of gaseous turbulent flames [13, 14, 45] that the PDF method usually yields lower peak mean temperature compared to models that do not consider turbulence-chemistry interactions. However, in this flame, the PDF model gives higher gas temperatures along the centerline. One reason is that the PDF model gives better mixing with the oxygen. Another reason is that more volatile gases are released and more carbon is burned downstream for the PDF model (Table 4). In contrast to turbulence-chemistry interactions in gaseous flames, here the interaction between the gas phase and the solid phase through temperature changes the total amount of fuel that is burned, and the result can be either higher or lower temperatures.

An important parameter for the PDF model is the mixing model constant

C_ϕ (the ratio of a turbulence velocity time scale to a turbulence scalar mixing time scale). In the limit $C_\phi \to \infty$, local fluctuations go to zero, and the model essentially reduces to the well-stirred reactor model discussed above. Here the value $C_\phi = 2$ is tested, compared to $C_\phi = 3$ in the baseline model. No discernable difference is found in gas-phase compositions/temperatures or in particle temperatures (not shown). This might be due to the fact that turbulence is relatively weak in this flame ($Re = 2,500$). From the discussion above, it can be concluded that it may be important to include a turbulence-chemistry interaction model, although the details of the model do not make a large difference here. Simulations and experiments of more fully turbulent flames will be needed to resolve this.

4.1.4. Interphase coupling models

Particle temperature and gas-phase mole fractions from two different source-distribution models (Model 1 and Model 3 in Section 3.3) are compared in Fig. 6. Results from both temperature-biased models are similar (Model 2 and Model 3), so only the results from Model 3 are presented here. Mean gas compositions obtained from coupling Model 1 and coupling Model 3 are nearly identical, while there are discernable differences in computed mean temperature for the solid phase, especially at downstream locations where oxygen has been completely depleted. Model 3 predicts higher temperature along the centerline than Model 1, which is reasonable because the source distribution is biased on temperature. The higher the notional particle temperature is, the more fuel and the more energy it will receive from the coal parcels, which makes the cell mean gas temperature higher, which in turn heats up the coal parcels even more. That this difference is more prominent at downstream locations might be a consequence of the fact that coal parcels produce larger mass/energy sources at downstream locations where temperatures are higher.

Numerically, Model 3 is more robust than Model 1, in terms of avoiding occurrences of unphysical notional particle temperatures. With the current available experimental data, it is difficult to judge which model is more appropriate in the pulverized coal combustion context. More studies and validation are needed regarding the source-distribution models, in particular in the framework of the transported composition PDF method.

The source-term coupling models might be improved further by separating the processes of heat transfer, devolatilization and surface reaction. In principle, each process could have a different dependence on the composition

variables. For example, devolatilization depends mainly on the local temperature, while surface reaction depends not only on the local temperature, but also local oxygen availability. Moreover, up to this point, the effects of turbulence-chemistry interactions have been accounted for in the gas-phase only, while source terms from the solid-phase are still collected based on the cell-mean temperature and composition. A potential improvement to the current model would be to introduce a "seen" temperature/composition for each solid parcel that is different from the cell-mean values, by sampling instantaneous temperature and composition from the gas-phase notional particles. This is left as a topic for future work.

4.1.5. Effects of finite-rate chemistry

Figure 7 compares results obtained using finite-rate chemistry with those obtained using a local equilibrium assumption. Here the WSR model has been used, to save computational time. It can be seen that the equilibrium solver predicts slightly lower gas and coal particle temperatures, and lower CO emission at upstream locations, compared to finite-rate chemistry. Finite-rate chemistry produces higher CO in fuel-rich regions. Zero CO is predicted before O_2 is completely depleted, which is not consistent with the experiments. As discussed in Section 4.1.1, the difference between results from the two models are more revealing than the absolute level of agreement with experiment. Thus, only the difference between the two cases are analyzed here.

Equilibrium gas-phase chemistry is widely assumed in pulverized coal simulations [39], based on the argument that gas-phase chemical reactions are much faster than devolatilization and surface reactions. Since devolatilization rates and surface reaction rates vary with coal type, heating rate and particle size, this assumption might not be valid in all cases. Moreover, chemical time scales are different for different species and the relative relationship between chemical time scale and devolatilization time scale also depends on the species of interest. To explore this, time-scale ratios can be examined. Damköhler number (Da) is the ratio of a turbulence time scale to a chemical time scale, and is an indicator of the extent to which turbulence-chemistry interactions are expected to be important. Similarly, the ratio of a turbulence time scale to a devolatilization time scale (denoted here as Da_{vol}) can serve as an indicator of the degree of interactions between turbulence and devolatilization. If the same definition for the turbulence time scale is used, then the ratio of Da_{vol} and Da is a measure of the relative rates of de-

volatilization and chemical reactions. The values of Da_{vol} and Da are plotted in Fig. 8, for each computational cell. Here the turbulence time scale is defined as $\tau_{turb} \equiv k/\varepsilon$. The chemical time scale is calculated as $\tau_{chem} \equiv \frac{\rho Y_\alpha}{R_\alpha}$, where R_α is the reaction rate for species α evaluated at cell-mean temperature and concentrations. C_2H_4 and H_2O are tested in this study to represent the fast chemistry and finite-rate chemistry present in flame A. It was shown in Section 4.1.1 that little surface reaction takes place in this flame. Thus, only devolatilization is considered in computing a time scale that is representative of the release of coal off-gas. The inverse of the devolatilization rate coefficient is used to define τ_{vol}, evaluated at the cell-mean temperature.

The diagonal of Fig. 8 corresponds to where the gas-phase chemical time scale τ_{chem} and the devolatilization time scale τ_{vol} are equal. In the upper left, the chemical time scale is larger than the devolatilization time scale; in this area, equilibrium chemistry would not be a valid assumption. In the lower right, the chemical time scale is smaller than the devolatilization scale, and an equilibrium chemistry assumption may be more appropriate. From the distributions in Fig. 8, it can be seen that the assumption of equilibrium chemistry is valid for the overall consumption rate of fuel (C_2H_4). However, if the production rate of H_2O or CO is of interest, the assumption of equilibrium chemistry is not expected to be valid at all locations. Moreover, the values of $\frac{\tau_{turb}}{\tau_{vol}}$ and $\frac{\tau_{turb}}{\tau_{chem}}$ are of order unity in much of the flame, based on the H_2O reaction rate. Thus, interactions between turbulence and gas-phase chemistry, and interactions between turbulence and devolatilization might be important. The time-scale results are consistent with the comparison of CO production between finite-rate chemistry and equilibrium chemistry in Fig. 7.

4.2. Flame B

The same baseline model has been applied to a second laboratory-scale coal jet flame (flame B), with modified parameters for the devolatilization model and the surface reaction model to account for the different coal composition. Baseline model results are discussed first. Then mixture-fraction statistics are examined, to test assumptions that have been made in earlier coal modeling studies.

4.2.1. Baseline model results

In the experiments, the air flow rate was held constant, while the loading of coal was changed to change the inlet stoichiometric ratio *sr* (Section 2).

Three distinct flame regions were identified from the experiments: isolated bright particles (IBP), the growing flame (GF) and the continuous flame (CF). Ignited particles in the IBP region are isolated and do not contribute to the growing of the flame, while in the GF region the ignited cloud is growing. In the CF region, the center of the jet is ignited stably. Following the practice used in [22], the stand-off distance of the coal flame is defined to be the axial position of the point where the local mean gas temperature first exceeds 1560 K, which is the start of the GF region for the time-averaged contour. Figure 9 shows the computed and measured stand-off distances for three different inlet stoichiometric ratios. It can be seen that the measured sensitivities of stand-off distance to inlet stoichiometric ratio are not captured with the baseline model. One reason is that the baseline devolatilization model does not capture the effect of different heating rates. For different coal loadings, the heating rate (essentially by the heated coflow) is different, and the rate of devolatilization is closely related to the heating rate. To explore this, results from a modified single-rate model that accounts for variations in heating rate proposed in [22] are also shown in Fig. 9. The six model parameters are obtained by fitting the devolatilization rates at two typical heating rates to the results produced by higher-fidelity devolatilization models. With this devolatilization model, the computed stand-off distances for $sr = 0.14$ and $sr = 0.22$ are within the confidence interval of the experimental measurements. However, there is still a discrepancy in the prediction for the smallest coal loading ($sr = 0.36$). For this case, no continuous flame region was observed in the experiments. The Reynolds number of this flame is 5,000 for cold flow, which is marginally turbulent. In [22], it was reported that a LES-based coal combustion model was able to reproduce the unsteady ignition that was reported in the experiment for $sr = 0.36$. It is not clear if a RANS-based model will be able to capture this, but at a minimum, it is expected that a better turbulence model would be necessary for this highly unsteady transitional flame.

Other aspects of the modeling where there is room for improvement include better knowledge of the coal properties (e.g., heating value of the coal), accounting for the temperature and composition dependence of the specific heat of the coal particles, and a better radiation model for the coal particles. It has been found that the standoff distances for the three different inlet stoichiometric ratios can be predicted within the confidence intervals of the experimental measurements by using different models/model parameters for each individual case (not shown). This emphasizes the importance of validat-

ing models across multiple conditions and multiple flames. This is especially important for coal simulation, because of the many individual subprocesses and complex interactions.

4.2.2. Mixture fraction statistics

As mentioned in Section 1, one advantage of a "high fidelity" model such as the present transported PDF/finite-rate chemistry model is that it can be exercised to provide guidance for developing simpler models. Here, key assumptions that have been made in mixture-fraction-based coal combustion models are examined, using statistics extracted from simulations for flame B. Because the fraction of coal undergoing surface reactions is very small in flame A, flame B is a more appropriate choice for this purpose. Following the definitions in [46], for each notional PDF particle, mixture fractions for devolatilization products and char oxidation products are defined as

$$f_{devol} = \frac{m_v}{m_v + m_p + m_s}, \tag{30}$$

$$f_{surf} = \frac{m_{ch}}{m_v + m_{ch} + m_p + m_s}, \tag{31}$$

where m_v, m_{ch}, m_p and m_s represent the mass of gas originating from devolatilization, surface reaction (char), the primary gas stream and the secondary gas stream, respectively. For the open flames considered here, the carrier air for the coal and the entrained surrounding air are considered to be the primary gas, while the secondary gas is considered to be the pilot flame for flame A or the hot combustion product stream for flame B. Figure 10 shows computed contours of mean and rms mixture fractions for the devolatilization products (f_{devol}) and the surface reaction products (f_{surf}) for flame B. It can be seen that as one moves downstream from the nozzle in the axial direction, f_{devol} peaks first, followed by f_{surf}. This is a consequence of the assumed sequential nature of the two processes, and is consistent with the fact that devolatilization is usually faster than surface reactions in coal-air combustion. The rms values show that there are turbulent fluctuations in both f_{devol} and f_{surf}. It is anticipated that the fluctuations will be even stronger for high-temperature oxy-coal combustion, where the surface reaction rates will be higher.

PDFs (histograms) of f_{devol} and f_{surf} at four points labeled in Fig. 10 are shown in Fig. 11. Fitted Beta distributions and clipped Gaussian distributions (based on the mean and rms values) are also shown. It can be seen from

Fig. 11 that distributions of f_{devol} and f_{surf} vary considerably with spatial location, with the relative importance of devolatilization and surface reaction processes. Surface reaction depends not only on the temperature, but also on oxygen availability. At downstream locations, both mixture fractions relax toward Gaussian distributions. However, near the nozzle and in the developing flame, the distributions take different shapes. The f_{devol} distribution is well represented as a clipped Gaussian distribution at all locations, while f_{surf} is less symmetric, and is better represented using a Beta function. For presumed-PDF models, a Beta function appears to be a reasonable choice. Another assumption that is usually made in mixture-fraction-based models is statistical independence of f_{devol} and f_{surf}. The computed correlation coefficients of f_{devol} and f_{surf} at the four locations are listed in Table 7. The value ranges from -1 near the nozzle to +1 at the outlet. Domino and Smith [47] have pointed out that the assumption of independent mixture fraction distributions is questionable, and the correlation coefficients calculated here support this conclusion. Contrary to the independent distribution assumption, at some locations in the flames, the correlation between these two mixture fractions is quite strong.

5. Conclusions

A transported PDF/finite-rate chemistry coal combustion model has been developed. The gas phase and solid phase are represented by two different sets of stochastic Lagrangian particles. Three different models are proposed to couple mass and energy transfer between the solid phase and the gas phase. Numerical simulations have been performed for two laboratory pulverized coal jet flames, and results have been compared with experimental measurements. The simulations include skeletal-level gas-phase chemical mechanisms, discrete dispersed-phase models (heat transfer, turbulent dispersion, devolatilization, surface reaction for coal parcels), radiation (a $P1$ model with gray properties), and a transported PDF method to account for gas-phase turbulent fluctuations in composition and temperature.

Quantitative comparisons with experiment are at least as good as any that have been reported in the literature to date with a RANS-based model. Systematic parametric model variations have been made to establish sensitivities and relative importance of various physical subprocesses. Comparisions of results from a well-stirred reactor model and the PDF model show differences in flame structure and temperature levels. Different interphase cou-

pling strategies also result in different computed temperature levels. These findings suggest that turbulence-chemistry interactions may be important in these flames. This is supported by analysis of time-scale ratios in the flame. Results for two different flames using the same models reveals both strengths and limitations of the model. For flame B, measured standoff heights for all three stoichiometries could not be reproduced using a single set of model parameters. With the limitations of the experimental data, it is difficult to draw definitive conclusions regarding which models are "better". Further parametric studies and validations are needed. At the same time, high quality experimental data with detailed measurements of particle temperature, velocity, and gas-phase concentrations are needed.

In addition to validation, the model has been exercised to check assumptions that are commonly invoked in simpler models. Analysis of the time scales for key processes suggest that finite-rate chemistry and turbulence-chemistry-particle interactions might be important. Mixture-fraction statistics generated from the model show that some assumptions that have been made in mixture-fraction-based coal models might be valid (e.g., presumed Beta distribution) while others are not (statistical independence of mixture fractions).

The accuracy of coal combustion prediction depends greatly on the choice of coal-related model parameters: devolatilization, in particular. More general devolatilization models, such as the chemical percolation devolatilization (CPD) model [48, 49, 50], or well-validated model parameters for the simpler devolatilization models, are expected to be necessary to give more reliable predictions. Surface reaction models that consider the the gasification reaction of CO_2 and H_2O and an elevated oxygen partial pressure should also be included for oxy-coal combustion. Radiation models have not been explored in this work, although radiation is expected to be important when clouds of coal particles are present, especially in high-temperature oxy-coal combustion environments. High-fidelity radiation models using spectral models will be implemented in the future, combined with the PDF method.

Acknowledgments

As part of the National Energy Technology Laboratory's Regional University Alliance (NETL-RUA), a collaborative initiative of the NETL, this technical effort was performed under the RES contract DE-FE0004000, and

also in part through instrumentation funded by the National Science Foundation through grant OCI-0821527. The authors thank Dr. E. D. Huckaby of NETL for helpful advice on aspects of coal combustion.

This project was funded by the Department of Energy, National Energy Technology Laboratory, an agency of the United States Government, through a support contract with URS Energy & Construction, Inc. Neither the United States Government nor any agency thereof, nor any of their employees, nor URS Energy & Construction, Inc., nor any of their employees, makes any warranty, expressed or implied, or assumes any legal liability or responsibility for the accuracy, completeness, or usefulness of any information, apparatus, product, or process disclosed, or represents that its use would not infringe privately owned rights. Reference herein to any specific commercial product, process, or service by trade name, trademark, manufacturer, or otherwise, does not necessarily constitute or imply its endorsement, recommendation, or favoring by the United States Government or any agency thereof. The views and opinions of authors expressed herein do not necessarily state or reflect those of the United States Government or any agency thereof.

References

[1] C. R. Shaddix, Combust. Flame 159 (2012) 3003–3006.

[2] C. R. Woodside, K. H. Casleton, J. Pepper, I. B. Celik, D. C. Haworth, E. D. Huckaby, O. A. Marzouk, T. Ochs, D. Oryshchyn, G. Richards, P. A. Strakey, J. Escobar-Vargas, X. Y. Zhao, International Pittsburgh Coal Conference, 2012.

[3] L. D. Smoot, D. T. Pratt (Eds.), Pulverized-coal combustion and gasification: theory and applications for continuous flow processes, Plenum Press, 1979. New York.

[4] L. D. Smoot, P. J. Smith (Eds.), Coal combustion and gasification, Plenum Press, 1985. New York.

[5] P. Edge, M. Gharebaghi, R. Irons, R. Porter, R. T. J. Porter, M. Pourkashanian, D. Smith, P. Stephenson, A. Williams, Chem. Eng. Res. Des. 89 (2011) 1470 – 1493.

[6] L. Chen, S. Z. Yong, A. F. Ghoniem, Prog. Energy Combust. Sci. 38 (2012) 156 – 214.

[7] T. Poinsot, D. Veynante, Theoretical and numerical combustion, Poinsot & Veynante, Toulouse, France. Available at http://elearning.cerfacs.fr/combustion/onlinePoinsotBook/buythirdedition/index.php, third edition, 2012.

[8] S. B. Pope, Prog. Energy Combust. Sci. 11 (1985) 119–192.

[9] P. J. Smith, T. H. Fletcher, Combust. Sci. and Technol. 58 (1988) 59–76.

[10] M. Rose, P. Roth, S. M. Frolov, M. G. Neuhaus, Combust. Sci. Technol. 149 (1999) 95–113.

[11] M. Stöllinger, B. Naud, D. Roekaerts, N. Beishuizen, S. Heinz, Combust. Flame 160 (2013) 384 – 395.

[12] M. Stöllinger, B. Naud, D. Roekaerts, N. Beishuizen, S. Heinz, Combust. Flame 160 (2013) 396 – 410.

[13] X. Y. Zhao, D. C. Haworth, E. D. Huckaby, Combust. Sci. Technol. 184 (2012) 676–693.

[14] X. Y. Zhao, D. C. Haworth, T. Ren, M. F. Modest, Combust. Theory Modell. 17 (2013) 354–381.

[15] L. Lu, S. B. Pope, J. Comput. Phys. 228 (2009) 361–386.

[16] S. M. Hwang, R. Kurose, F. Akamatsu, H. Tsuji, H. Makino, M. Katsuki, Energy Fuels 19 (2005) 382–392.

[17] A. Bermudez, J. L. Ferrin, A. Linan, L. Saavedra, Combust. Flame 158 (2011) 1852–1865.

[18] B. M. Franchetti, F. C. Marincola, S. Navarro-Martinez, A. M. Kempf, Proc. Combust. Inst. 34 (2013) 2419–2426.

[19] N. Hashimoto, R. Kurose, H. Shirai, Fuel 97 (2012) 277–287.

[20] O. T. Stein, G. Olenik, A. Kronenburg, F. C. Marincola, B. M. Franchetti, A. M. Kempf, M. Ghiani, M. Vascellari, C. Hasse, Flow Turbul. Combust. 90 (2013) 859–884.

[21] M. Taniguchi, H. Okazaki, H. Kobayashi, S. Azuhata, H. Miyadera, J. Energy Resour. Technol. 123 (2001) 32–38.

[22] K. Yamamoto, T. Murota, T. Okazaki, M. Taniguchi, Proc. Combust. Inst. 33 (2011) 1771–1778.

[23] OpenFOAM, 2013. http://www.openfoam.com.

[24] C. Crowe, D. Stock, M. Sharma, J. Fluids Eng. 99 (1977) 325–332.

[25] S. Subramaniam, S. B. Pope, Combust. Flame 115 (1998) 487–514.

[26] R. L. Curl, AIChE J. 9 (1963) 175–181.

[27] L. Zhou, Theory and numerical modeling of turbulent gas-particle flows and combustion, Science Press and CRC Press INC, 1993.

[28] A. D. Gosman, E. Ioannides, J. Energy 7 (1983) 482–490.

[29] H. Kobayashi, J. B. Howard, A. F. Sarofim, Proc. Combust. Inst. 16 (1977) 411–425.

[30] S. Badzioch, P. G. W. Hawksley, Ind. Eng. Chem. Process Des. Develop. 9 (1970) 521–530.

[31] M. M. Baum, P. J. Street, Combust. Sci. Technol. 3 (1971) 231–243.

[32] J. J. Murphy, C. R. Shaddix, Combust. Flame 144 (2006) 710–729.

[33] D. C. Haworth, Prog. Energy Combust. Sci. 36 (2010) 168–259.

[34] E. H. Kung, PDF-based modeling of autoignition and emissions for advanced direct-injection engines, Ph.D. thesis, University Park, PA, 2008.

[35] C. T. Bowman, R. K. Hanson, D. F. Davidson, W. C. Gardiner, V. Lissianski, G. P. Smith, D. M. Golden, M. Frenklach, M. Goldenberg (1995). GRI-Mech 2.11; Available at http://www.me.berkeley.edu/gri_mech.

[36] R. S. Mehta, D. C. Haworth, M. F. Modest, Proc. Combust. Inst. 32 (2009) 1327 – 1337.

[37] D. W. Shaw, X. Zhu, M. K. Misra, R. H. Essenhigh, Proc. Combust. Inst. 23 (1990) 1155–1162.

[38] R. S. Barlow, Intern'l. Workshop on Measurement and Computation of Turbulent Nonpremixed Flames, 2011. Combustion Research Facility, Sandia National Laboratories, Livermore, CA; http://www.ca.sandia.gov/TNF/.

[39] J. Pedel, J. N. Thornock, P. J. Smith, Combust. Flame 160 (2013) 1112–1128.

[40] I. Petersen, J. Werther, Chem. Eng. Process. 44 (2005) 717–736.

[41] S. James, M. S. Anand, M. K. Razdan, S. B. Pope, J. Eng. Gas Turbines Power 123 (2001) 747–756.

[42] J. M. Maclnnes, F. V. Bracco, Phys. Fluids A 4 (1992) 2809–2824.

[43] J. D. Smith, P. J. Smith, S. C. Hill, AICHE J. 39 (1993) 1668–1679.

[44] B. S. Brewster, L. L. Baxter, L. D. Smoot, Energy Fuels 2 (1988) 362–370.

[45] J. Jaishree, D. C. Haworth, Combust. Theory Modell. 16 (2012) 435–463.

[46] D. V. Flores, T. H. Fletcher, Combust. Sci. Technol. 150 (2000) 1–26.

[47] S. P. Domino, P. J. Smith, Proc. Combust. Inst. 28 (2000) 2329–2336.

[48] D. M. Grant, R. J. Pugmire, T. H. Fletcher, A. R. Kerstein, Energy Fuels 3 (1989) 175–186.

[49] T. H. Fletcher, A. R. Kerstein, R. J. Pugmire, D. M. Grant, Energy Fuels 4 (1990) 54–60.

[50] T. H. Fletcher, A. R. Kerstein, R. J. Pugmire, M. S. Solum, D. M. Grant, Energy Fuels 6 (1992) 414–431.

[51] E. H. Chui, P. Hughes, G. Raithby, Combust. Sci. Technol. 92 (1993) 225–242.

Table 1: Inlet specifications for flame A.

Coal feed rate	1.49×10^{-4} kg/s
Air flow rate	1.80×10^{-4} m^3/s
Methane flow rate	2.33×10^{-5} m^3/s

Table 2: Coal properties for flame A. [a] Dry basis. [b] As received.

Proximate analysis (wt%)	
Moisture[a]	2.6
Volatile matter[b]	26.90
Fixed carbon[b]	57.9
Ash[b]	15.2
Ultimate analysis (wt%)	
Carbon[b]	71.9
Hydrogen[b]	4.4
Nitrogen[b]	1.5
Oxygen[b]	6.53
Sulfur[b]	0.44
Higher heating value	29.1 MJ/kg
Lower heating value	28.1 MJ/kg

Table 3: Baseline physical models and numerical parameters for flame A.

Item	Model	Baseline values
Eulerian CFD	Unstructured finite-volume method	Axisymmetric 9,660 cells
Turbulence closure	$k-\varepsilon$	$C_\mu = 0.09$, $C_{\varepsilon 1} = 1.60$, $C_{\varepsilon 2} = 1.92$, $\sigma_k = 1.0$, $\sigma_\varepsilon = 1.3$
Wall turbulence	Standard wall function	$\kappa = 0.4187$, $E = 9.8$
TCI closure	transported PDF model	35 particles per cell
Mixing model	EMST model	$C_{mix} = 3$
Source redistribution model	Model 3 ($exp(-C/T_p)$)	$C = 5,000$ K
Turbulent fluxes	Gradient transport	Turbulent Schmidt and Prandtl numbers $Sc_T = Pr_T = 1$
Gas-phase chemistry	ABF 31-species [36]	-
Gas-phase radiative properties	Grey gas and particles	Scattering calculated as in [51], $\varepsilon_{gas} = 0.075$, $\varepsilon_{coal} = 0.85$
Devolatilization	Two-rates model	$A_1 = 2.0 \times 10^5$ 1/s, $E_1 = 1.05 \times 10^8$ J/kmol-K, $\alpha_1 = 0.3$, $A_2 = 1.3 \times 10^7$ 1/s, $E_2 = 1.67 \times 10^8$ J/kmol-K, $\alpha_2 = 1.0$
Surface reaction	Diffusion-kinetic control model	$A = 0.011$ (kg/m^2-s)(N/m^2), $E = 5.0 \times 10^7$ J/kmol-K, $Sb = 1.0$
coal properties	constant volume, constant char and ash specific heat	$cp_{char,ash} = 710$ J/kg-K

Table 4: Total released combustibles (mass per 1 kg dry coal) for flame A.

	released volatiles (%)	burned char (%)
Baseline model	0.16	0.00
Experiment	0.12	0.065

Table 5: Variations in coal combustion models for flame A.

Case 1	Baseline model (Table 3), except with WSR replacing PDF for gas phase
Case 2	Single-rate devolatilization ($A_1 = 4474$ 1/s, $E_1 = 1.92 \times 10^7$ J/kmol [18, 19, 20])
Case 3	$cp_{ash} = 1000$ J/kg-K, $cp_{char} = 1500$ J/kg-K
Case 4	Retention energy (char combustion energy 100% retained)
Case 5	Concurrent devolatilization and surface reaction
Case 6	Volatile matter composition ($Q = 1$)

Table 6: Effects of model variations.

case no.	max. $\tilde{T}$ (K)	centerline location (mm) where $Y_{O_2} = 0$	released VM (%)	gasified char (%)
Case 1	1360	105	17	0.07
Case 2	1270	45	40	3.0
Case 3	1320	120	14.7	0
Case 4	1350	105	17.0	1.0
Case 5	1350	103	16.8	3.0
Case 6	1345	∞	6.8	0

Table 7: Computed mixture-fraction correlation coefficients (f_{devol} and f_{surf}) for flame B at four locations.

Location	Point 1	Point 2	Point 3	Point 4
correlation coefficient	-0.99	-0.8	0.32	0.90

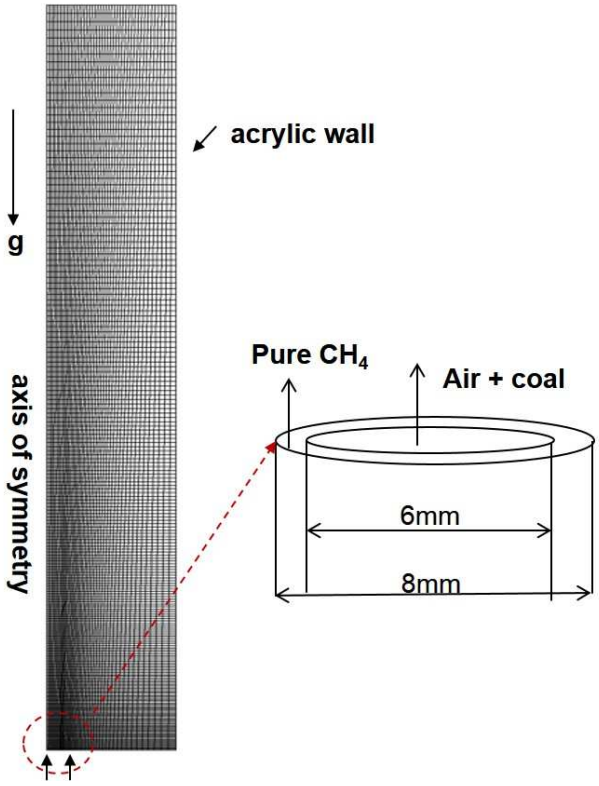

Figure 1: 2D sketch of flame A, with inlet nozzle and mesh details.

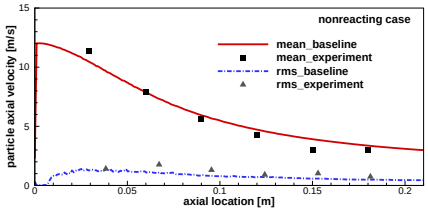

(a) Centerline mean and rms axial particle velocity profiles

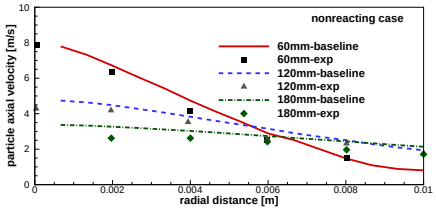

(b) Radial profiles of mean axial particle velocity at three axial locations

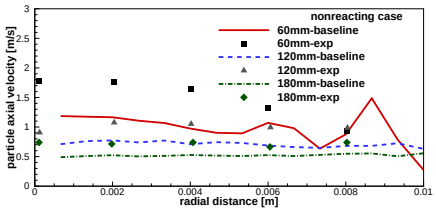

(c) Radial profiles of rms axial particle velocity at three axial locations

Figure 2: Computed and measured mean and rms axial particle velocity profiles for nonreacting flame A configuration.

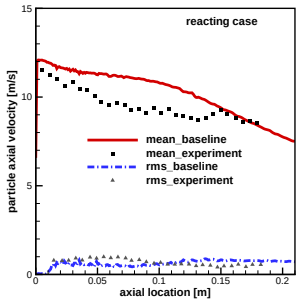

(a) Mean and rms axial particle velocity

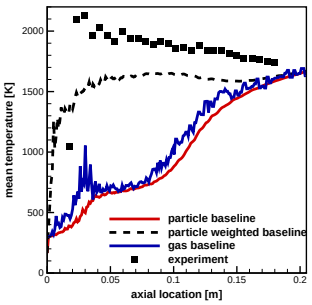

(b) Mean temperature

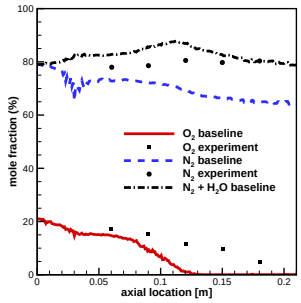

(c) Mean O_2 and N_2 mole fraction

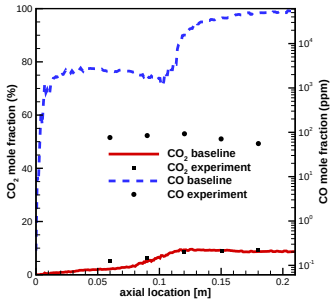

(d) Mean CO and CO_2 mole fraction

Figure 3: Computed and measured centerline profiles for flame A. a) Mean and rms particle axial velocity. b) Mean particle temperature. c) Mean O_2 and N_2 mole fractions. d) Mean CO and CO_2 mole fractions.

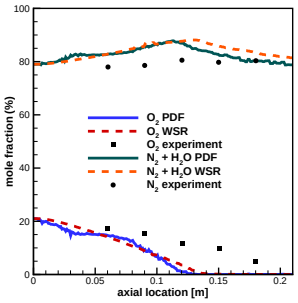

(a) Mean O_2 and N_2 mole fractions

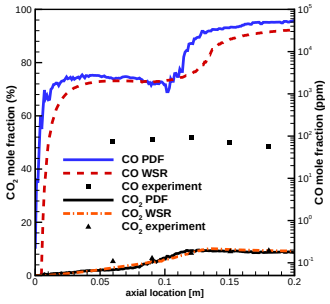

(b) Mean CO_2 and CO mole fractions

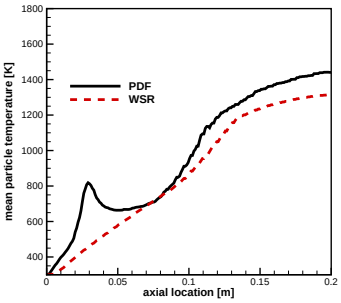

(c) Mean particle temperature

Figure 4: Computed (WSR versus PDF models) and measured centerline profiles of mean gas-phase species mole fractions and particle temperature for flame A.

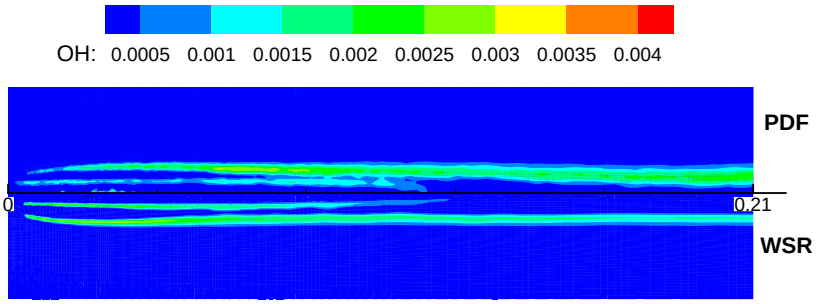

Figure 5: Computed (WSR versus PDF models) mean OH mass fraction contours for flame A.

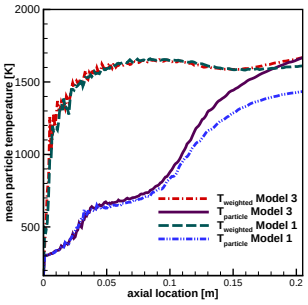

(a) Mean particle temperature

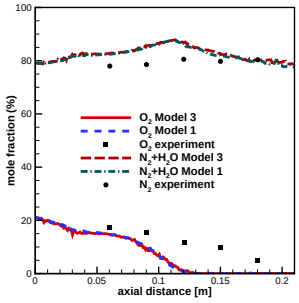

(b) Mean O_2 and N_2 mole fractions

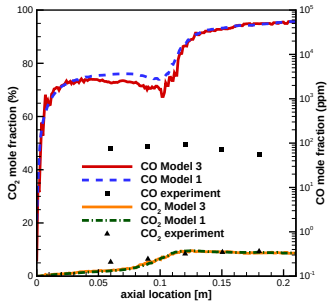

(c) Mean CO_2 and CO mole fractions

Figure 6: Computed (two different interphase coupling strategies: Model 1 versus Model 3) centerline profiles of mean particle temperature and gas-phase composition for flame A.

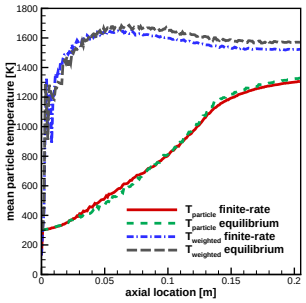

(a) Mean gas temperature

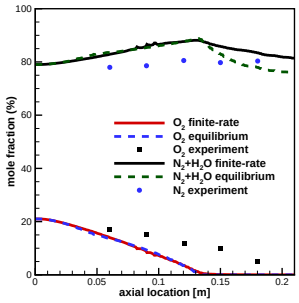

(b) Mean O_2 and N_2 mass fraction

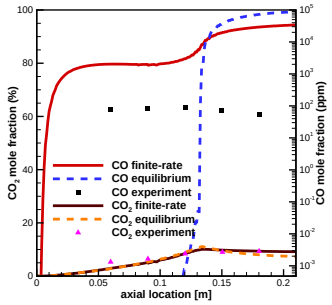

(c) Mean CO and CO_2 mass fraction

Figure 7: Computed (finite-rate chemistry versus equilibrium chemistry) centerline profiles of mean particle temperature and gas-phase composition for flame A.

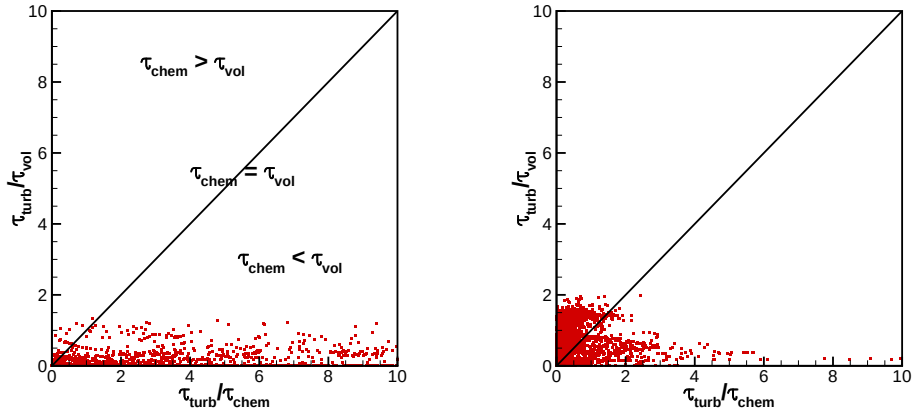

(a) Computed time-scale ratios for C_2H_4

(b) Computed time-scale ratios for H_2O

Figure 8: Computed time-scale ratios for all cells for flame A.

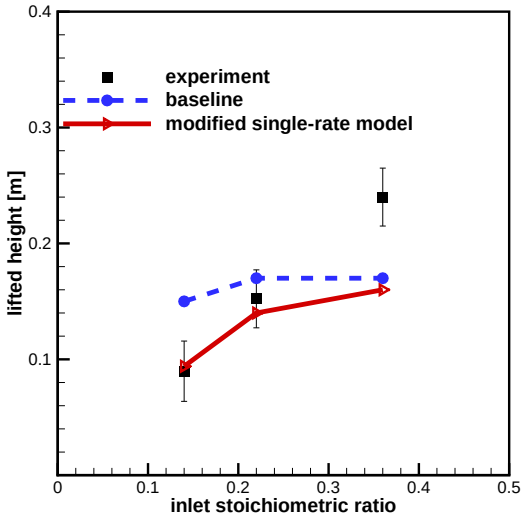

Figure 9: Computed (baseline model and a modified single-rate model) and measured stand-off distances for three inlet stoichiometric ratios for flame B.

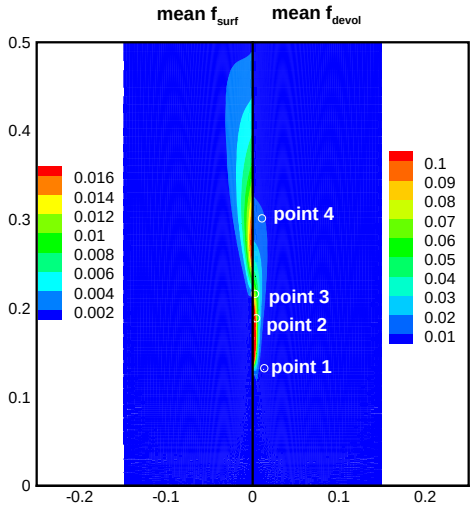

(a) Mean mixture fractions

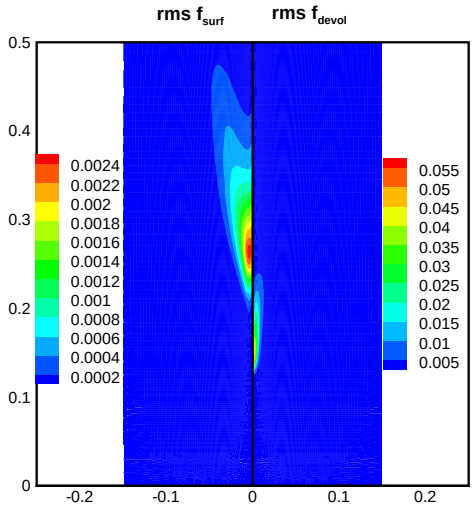

(b) Rms mixture fractions

Figure 10: Computed mean and rms mixture fraction contours for flame B.

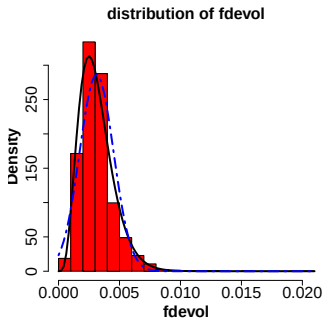

(a) f_{devol} at point 1

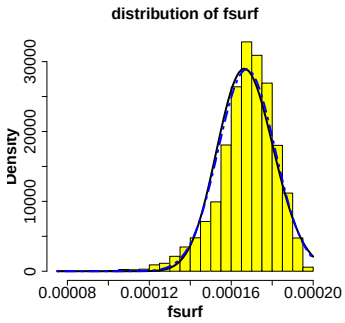

(b) f_{surf} at point 1

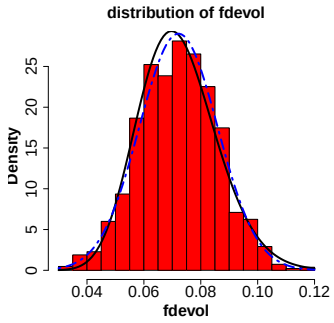

(c) f_{devol} at point 2

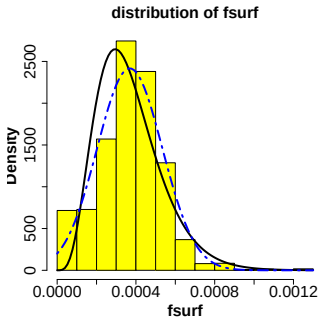

(d) f_{surf} at point 2

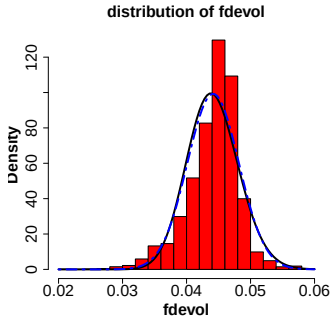

(e) f_{devol} at point 3

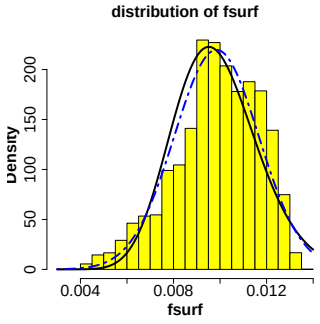

(f) f_{surf} at point 3

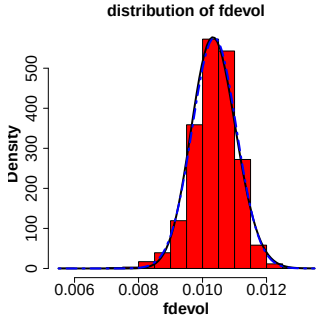

(g) f_{devol} at point 4

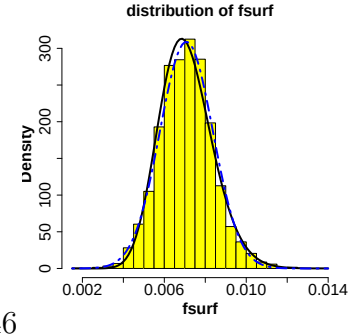

(h) f_{surf} at point 4

Figure 11: Histograms and fitted Beta and clipped Gaussian distributions for f_{devol} and f_{surf} at four locations in flame B. Black lines represent Beta distributions and blue dashed lines represent clipped Gaussian distributions.